Nano Research

Open Access

Research Article

An *in-situ* zincophilic and water-shielding interface for durable aqueous zinc-ion battery

Lei Xu[1], Hong Luo[1,2], Yi Lin[1,2,4] ✉, and Yi Guo[3] ✉

[1] College of Materials Science and Engineering, Sichuan University of Science & Engineering, Zigong 643000, China
[2] Material Corrosion and Protection Key Laboratory of Sichuan Province, Sichuan University of Science & Engineering, Zigong 643000, China
[3] College of Optoelectronic Engineering, Chengdu University of Information Technology, Chengdu 610103, China
[4] Leshan West Silicon Materials Photovoltaic New Energy Industry Technology Research Institute, Leshan Normal University, Leshan 614000, China

Cite this article: *Nano Research*, **2026**, *19*, 94908690. https://doi.org/10.26599/NR.2026.94908690

ABSTRACT: Aqueous zinc-ion batteries (AZIBs) are plagued by water-rich and unstable electrolyte/electrode interface, which results in poor reversibility and short lifespan. Herein, trace sodium perfluorononyloxybenzenesulfonate (OBS) and bismuth potassium citrate (BPC) additives collaboratively construct a zincophilic and water-shielding interface. Both OBS and BPC molecules preferentially adsorb on the Zn anode, forming a H_2O-blocking layer to suppress water-induced side reactions. Concurrently, upon cycling, OBS decomposes and forms ZnF_2 with high ionic conductivity, while Bi^{3+} derived from BPC is electrochemically reduced to metallic Bi^0, serving as zincophilic nucleation sites. This *in-situ* formed ZnF_2/Bi-modified interface synergistically regulates Zn^{2+} flux and homogenizes the interfacial electric field. Consequently, the Zn||Zn symmetric cell achieves exceptional cycling stability over 6600 h at 1 mA·cm^{-2} and 1 mAh·cm^{-2}, and a lifespan over 1000 h at high current density and areal capacity (3 mA·cm^{-2} and 3 mAh·cm^{-2}). The full cell paired with $NH_4V_4O_{10}$ cathode delivers a capacity retention of 95.54% after 500 cycles at 1 A·g^{-1}, substantially outperforming the baseline electrolyte. This streamlined strategy *in-situ* constructs a multifunctional hybrid interphase, paving a new way for durable and high-performance AZIBs.

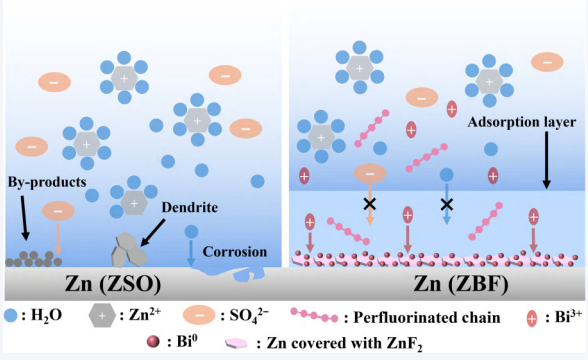

KEYWORDS: electrolyte additive, chemisorption, water-shielding and zincophilic interface, planar growth

1 Introduction

The growing global dependence on fossil fuels has led to energy insecurity due to resource depletion and geopolitical instability, as well as environmental pollution primarily from greenhouse gas emissions. Although renewable energy sources offer clean and sustainable alternatives, their intermittency and geographical limitations pose challenges for large-scale industrial implementation [1]. Consequently, the development of efficient and reliable electrochemical energy storage systems is critical for enabling the grid-scale deployment of renewable energy sources. Aqueous zinc-ion batteries (AZIBs) have emerged as a promising candidate for grid-scale energy storage applications owing to high theoretical capacity (820 mAh·g^{-1} and 5885 mAh·cm^{-3}), low redox potential (−0.76 V vs. standard hydrogen electrode (SHE)), and the inherent electrochemical stability of zinc metal in ambient conditions [2].

However, the Zn anode suffers from rampant dendrite growth and side reactions during electrochemical cycling, which degrades the cycling stability of AZIBs and impedes their practical application [3]. Specifically, (i) the heterogeneous electric field distributions across the Zn anode, combined with two-dimensional (2D) diffusion of Zn^{2+}, intensify the tip effect and thereby accelerate the dendrite growth. These dendrites may penetrate the separator, causing internal short circuits [4]. (ii) Hydroxide ions (OH^-) generated from water-splitting reactions (e.g., hydrogen evolution reaction (HER)) during cycling trigger irreversible corrosion, forming insulating zinc hydroxysulfate hydrate (ZHS, $Zn_4SO_4(OH)_6{\cdot}xH_2O$) passivation layers. This process consumes active material, increases interfacial impedance, and degrades both the capacity and Coulombic efficiency (CE) [5]. ZHS accumulation progressively reduces the electroactive sites for Zn^{2+}

Received: January 19, 2026; **Revised:** March 15, 2026
Accepted: March 28, 2026

✉Address correspondence to Yi Lin, llinyi@163.com; Yi Guo, guoyilala@cuit.edu.cn

electrodeposition, which in turn promotes further dendrite growth, establishing a detrimental feedback loop. Additionally, HER constrains the thermodynamic electrochemical stability window of aqueous electrolytes (~ 1.23 V), fundamentally limiting the achievable energy density of AZIBs [6]. Therefore, stabilizing electrode/electrolyte interface is essential for enhancing the cycling stability and energy density of AZIBs.

To overcome these aforementioned challenges, researchers have pursued Zn anode modification and electrolyte engineering, including anode surface alloying [7], protective coating fabrication [8], three-dimensional (3D) structure design [9], novel electrolyte formulations [10], electrolyte additive incorporation [11], and high concentration electrolyte optimization [12]. A critical objective common to these approaches is the regulation of the electrode/electrolyte interface, whose properties are critically dependent on the electrolyte composition. As the continuous medium for ion transport and the direct participant in interfacial reactions, the electrolyte's chemical composition and concentration fundamentally determine the Zn^{2+} solvation structure, transport kinetics, and deposition behavior [13]. Therefore, electrolyte optimization, particularly via functional additives, represents a promising and efficient strategy to enhance the electrochemical performance of AZIBs.

Generally, the functional additives employed in the electrolyte are primarily divided into organic additives and metal ion additives according to their chemical characteristics. Organic additives, such as tetra-n-butylammonium sulfate (TBA_2SO_4), sodium dodecyl sulfate (SDS), and sodium dodecyl benzene sulfonate (SDBS), play multiple roles toward stabilizing the cycling performance of AZIBs, including stabilizing the electrode/electrolyte interface, modulating Zn^{2+} solvation structures, enhancing ionic conductivity, and improving electrolyte thermal stability [14–16]. For the metal ion additives, metal cations (e.g., Ce^{3+}, Y^{3+}, La^{3+}, and Na^{+}) regulate Zn^{2+} flux at the anode surface via the electrostatic shielding mechanism, thereby inducing homogeneous Zn nucleation [17–20]. In addition, metal ion additives can form protective interfacial layers on the anode surface, effectively mitigating side reactions, such as HER and corrosion. Despite enhancing the cycling stability and performance of AZIBs, the electrolyte additive strategy exhibits inherent limitations that need to be addressed. Firstly, organic additives may induce environmental pollution risks. These additives may decompose or fail under elevated temperatures, which potentially compromise battery safety and cycling stability [21]. Moreover, metal ion additives may trigger side reactions with other components of the electrolyte, resulting in the destabilization of the electrolyte, which in turn leads to ionic conductivity imbalances at elevated concentrations [22]. Beyond the above limitations, the efficacy of additives is fundamentally dominated by their intrinsic physicochemical characteristics. Specifically, high solubility and a zincophilic nature are critical for additives to effectively regulate the Zn^{2+} flux and suppress the side reactions at the electrode/electrolyte interface. Therefore, systematic multi-criteria screening of electrolyte additives with respect to cost-effectiveness, long-term electrochemical stability, and safety characteristics, integrated with in-depth mechanistic elucidation of their functional behavior, is imperative for enhancing the cycling stability of AZIBs.

Compared with conventional electrolytes, fluorinated electrolytes exhibit several distinct advantages. Firstly, leveraging the high electronegativity of fluorine, fluorinated compounds facilitate the formation of robust fluoride interphase layers (e.g., ZnF_2) on Zn anodes. This imparts exceptional chemical/electrochemical stability, which effectively suppresses dendritic growth, blocks the access of H_2O molecules to the anode, and mitigates HER as well as corrosion side reactions [23]. Secondly, fluorinate anions (e.g., $C_4F_9SO_3^-$, BF_4^-, and bis(trifluoromethanesulfonyl)imide ($TFSI^-$)) reconfigure Zn^{2+} solvation structures via preferential coordination, thereby lowering the desolvation energy barriers to optimize deposition kinetics and promote uniform nucleation [24–26]. Thirdly, fluorinated components suppress cathode dissolution and electrolyte decomposition by reducing water activity and expanding the operational electrochemical stability window [27]. Additionally, fluorinated components enhance electrolyte wettability on Zn electrodes and accelerate Zn^{2+} transport [28]. Collectively, these mechanisms enable synergistic optimization of electrode/electrolyte interface stability, ion transport kinetics, and bulk chemical stability through *in-situ* interfacial construction and solvation sheath reorganization, establishing a new design direction for high-performance zinc-based energy storage systems. For example, Zhao et al. [29] introduced perfluorooctanoic acid (PFOA) to $ZnSO_4$ (ZSO) electrolyte, which resulted in the formation of an adsorbed layer of perfluorinated n-octyl chains on Zn anode. The strongly negatively charged perfluoroalkyl chains in this layer redistributed Zn^{2+} flux near the electrode/electrolyte interface through electrostatic repulsion, eliminating uneven charge distribution caused by the "tip effect". Simultaneously, SO_4^{2-} migration toward the Zn anode was suppressed, significantly enhancing corrosion resistance. These synergistic effects collectively enabled Zn||Zn symmetric cells to achieve a 2200 h cycle life at 1 mA·cm^{-2}. Xu et al. [23] demonstrated that the composite electrolyte of $Zn(CF_3SO_3)_2$ with methanol transformed the Zn^{2+} solvation structures from $[Zn(H_2O)_6]^{2+}$ to $[Zn(H_2O)_2(CH_3OH)_2]^{2+}$, delivering methanol-dominated species to the electrode/electrolyte interface to minimize water contact with the Zn anode. Concurrently, $Zn(CF_3SO_3)_2$ induced the formation of a fluoride-rich interface (ZnF_2) on the Zn anode that promoted the preferential growth of Zn (002) planes during electrodeposition. The combined effect of methanol-dominated interfaces and crystallographic control afforded an ultra-long cycle life exceeding 1000 h at 40 mA·cm^{-2} to Zn||Zn symmetric cells. Guo et al. [30] designed an electrolyte system with high F/O atom ratio by employing hexafluoro isopropanol (HFIP) as a fluorinated cosolvent, effectively minimizing interfacial side reactions. Simultaneously, HFIP facilitated the construction of a ZnF_2-rich solid electrolyte interphase (SEI), inducing homogeneous deposition of Zn on the anode. Benefiting from this dual modification, Zn||Zn symmetric cells exhibited 3200 h of cycling stability at 1 mA·cm^{-2}. Chen et al. [31] constructed a low coordination number solvation structure ($[Zn(H_2O)_2(EG)_2(otf)_2]$) using ethylene glycol (EG) and zinc trifluoro sulfonate (Znotf, where otf denotes trifluoromethanesulfonate) to reduce the free water content. Such a low-coordination solvation structure afforded stable cycling of 4500 h for Zn||Zn symmetric cells at 1 mA·cm^{-2}.

The design principle of multi-mechanistic synergy extends to the application of metal cation additives for optimizing AZIBs performance. These additives operate through several key mechanisms. Firstly, facilitating uniform Zn^{2+} electrodeposition via the electrostatic shielding effect. Moreover, modifying Zn^{2+} solvation structures to reduce active water molecules content within the inner solvation sphere, which is beneficial in suppressing HER.

Furthermore, constructing protective SEI with high ionic conductivity on the anode to restrain the electrolyte-induced corrosion.

Notably, bismuth (Bi)-ion additives and their corresponding reduction product, metallic Bi, constitute an exemplary system that achieves the synergistic optimization by virtue of their unique electrochemical properties. Specifically, the Bi^{3+}(aq)/Bi(s) redox couple exhibits a higher reduction potential (+0.32 V vs. SHE) than Zn^{2+}(aq)/Zn(s) (−0.76 V vs. SHE), which drives the preferential electrodeposition of Bi onto the Zn anode. The resultant deposited Bi layer plays a triple role in enhancing the electrochemical properties of AZIBs. At first, it modulates the Helmholtz-layer diffusion field via electrostatic shielding, enabling spatially uniform Zn^{2+} concentration gradients near the anode surface and facilitating homogeneous Zn^{2+} flux transport from bulk electrolyte. Secondly, intrinsic zincophilicity of Bi atoms can provide numerous nucleation sites across the anode surface for uniform deposition of Zn [32, 33]. Furthermore, Bi exhibits sluggish HER kinetics compared to that of Zn in the acidic condition, which effectively suppresses HER on the anode during Zn^{2+} electroplating process [34]. It should be noted that Bi is environmentally benign and possesses a significantly lower production cost than metals, such as Cu, Ni, Sn, and Ag [35]. Therefore, Bi-based additives demonstrate significant advantages in stabilizing Zn anode interface. For example, Guo et al. [36] constructed an artificial Bi-based protective layer on Zn anode via a displacement reaction using $Bi(CF_3SO_3)_3$ in 1,2-dimethoxyethane, which extended cycle life of Zn||Zn symmetric cells by a factor of 3.5. Zhao et al. [33] developed a Bi@Zn interface with a porous 2D interconnected nanosheet structure. This architecture homogenized Zn^{2+} flux distribution and enhanced Zn^{2+} migration kinetics, thereby facilitating rapid and uniform nucleation of Zn hexagonal crystals. The Zn||Zn symmetric cells thus achieve a cycle life of 2000 h at 10 mA·cm^{-2}. Wang et al. [37] fabricated an *in-situ* Bi-based activation layer on the Zn anode by a displacement reaction, which enhanced the corrosion resistance of anode and afforded abundant nucleation sites for uniform Zn^{2+} electrodeposition. Ye et al. [38] designed a Bi-Bi_2O_3-loaded carbon nanofiber (Bi-Bi_2O_3@CNF) interlayer on the Zn anode. The electrostatic shielding effect from Bi-Bi_2O_3 promoted uniform Zn deposition, suppressed dendrite growth and side reactions, and alleviated the electrode polarization, thus allowing Zn||Zn symmetric cells to maintain stable cycling for over 200 h at 20 mA·cm^{-2}.

To integrate these merits into a single system, we propose a novel dual-additive electrolyte strategy. This is realized by introducing trace amounts of environmentally benign sodium perfluorononyloxybenzenesulfonate (OBS, 600 ppm) and bismuth potassium citrate (BPC, 7 ppm) into a baseline 2 M $ZnSO_4$ electrolyte, forming a multifunctional electrolyte denoted as ZBF. We demonstrate that OBS and BPC operate through synergistic yet distinct mechanisms to construct a multifunction hybrid interphase on the Zn anode. First, their co-adsorption forms a dense, H_2O-blocking layer that significantly mitigates corrosion. During cycling, this interface evolves *in-situ*: OBS facilitates the formation of ZnF_2, which enhances interfacial ion transport, while Bi^{3+} from BPC is electrochemically reduced to metallic Bi^0, providing zincophilic nucleation sites to guide deposition. Coupled with improved electrolyte wettability and a reduced Zn^{2+} desolvation barrier, this multifunctional interphase synergistically regulates ion flux and homogenizes the electric field, effectively suppressing dendrite growth and HER. As a result, Zn||Zn symmetric cells with the ZBF electrolyte achieve an ultralong cycling lifespan over 6600 h at 1 mA·cm^{-2} and 1 mAh·cm^{-2}, and Zn||$NH_4V_4O_{10}$ full cells retain 95.54% capacity after 500 cycles at 1 A·g^{-1}. This work provides a rational and effective electrolyte design paradigm, highlighting the great potential of synergistic interfacial engineering for developing practical, high-performance AZIBs.

2 Result and discussion

2.1 Constructing a hybrid functional adsorption Layer

Trace OBS and BPC are used as functional additives to stabilize the Zn anode, and corresponding mechanism of action is investigated. The change in electrolyte/electrode interface is investigated by the interface electric double layer (EDL). As shown in Fig. 1(a) and Fig. S1 in the Electronic Supplementary Material (ESM), EDL capacitance value significantly decreases with the addition of OBS and BPC. This reduction proves that additives preferentially adsorb onto the Zn surface, effectively reducing the contact between free H_2O molecules and the Zn electrode, thereby suppressing corrosion and associated side reactions. The surface chemical bonding states of Zn foils were investigated using Fourier transform infrared (FTIR) reflectance spectroscopy after 7 days of immersion in the electrolyte. As shown in Fig. 1(b), the FTIR spectrum of the Zn foil immersed in ZBF electrolyte exhibited characteristic peaks at about 1239 and 1296 cm^{-1}, corresponding to the asymmetric stretching vibrations of –CF_2– and –CF_3– groups [39], respectively, suggesting the adsorption of perfluorinated chain segments from OBS molecules onto the Zn surface. Moreover, absorption peaks were observed at around 1493 and 1592 cm^{-1}, which can be assigned to the asymmetric stretching vibration of –COO– [40], indicating the carboxyl groups (–COOH) of BPC molecules interact with and adsorb onto the Zn foil surface. These results demonstrate that OBS and BPC molecules in ZBF electrolyte selectively adsorb onto the Zn surface, thereby promoting the formation of an organic adsorption layer at the electrode/electrolyte interface. To further validate the adsorption feasibility of OBS/BPC on the Zn anode, the molecular energy levels were investigated by density functional theory (DFT) simulations. The highest occupied molecular orbital (HOMO) energy levels of OBS and BPC are higher (less negative) than those of H_2O (Fig. S2 in the ESM), indicating a stronger tendency to donate electrons. Combined with their narrower HOMO–lowest unoccupied molecular orbital (LUMO) gaps (6.04 and 4.94 eV for OBS and BPC, respectively, vs. 9.97 eV for H_2O), this suggests enhanced reactivity and favorable adsorption onto the Zn anode.

To further elucidate the composition and chemical states of this interfacial layer, X-ray photoelectron spectroscopy (XPS) measurement was conducted on Zn electrodes after 7 days of immersion in ZBF electrolyte (Fig. 1(c) and Fig. S3 in the ESM). The survey spectrum reveals characteristic Bi 4f, C 1s, and F 1s peaks. Deconvolution of the Bi 4f spectrum shows doublet peaks at 160.38 eV (Bi $4f_{7/2}$) and 163.72 eV (Bi $4f_{5/2}$) with a spin-orbit splitting of 3.34 eV, which is consistent with metallic bismuth (Bi^0) [36]. These results consist of the X-ray diffraction (XRD) results. Deconvolution of the C 1s spectrum reveals three components at 293.38 eV (–CF_3), 286.57 eV (C–O), and 284.73 eV (C–C), all of which are consistent with OBS adsorption [39]. The high-resolution F 1s spectrum exhibits two distinct peaks. The one at 688.88 eV,

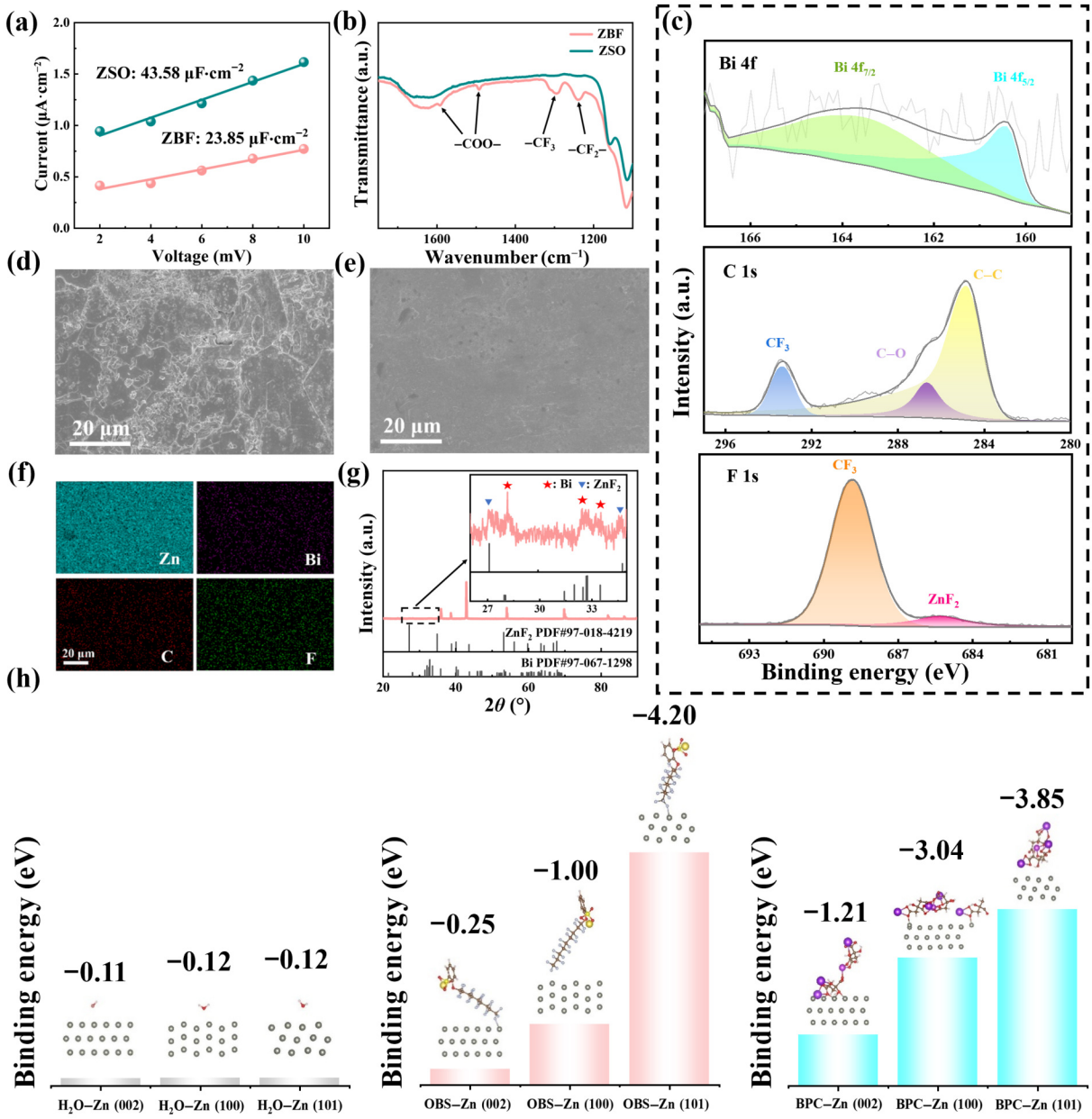

Figure 1 (a) EDL capacitance of Zn||Zn symmetric cells in ZSO and ZBF electrolytes. (b) FTIR spectra of the Zn foil after 7 days of immersion in ZSO and ZBF electrolytes. (c) XPS spectra of Zn electrodes after 7 days of immersion in ZBF electrolyte. ((d) and (e)) Corresponding surface morphologies of Zn electrodes after 7 days immersion in ZSO and ZBF electrolytes. (f) EDS patterns of Zn electrodes after 7 days of immersion in ZBF electrolyte. (g) XRD pattern of Zn electrodes after 1200 h of cycling in ZBF electrolyte. (h) The adsorption energies of H_2O, OBS, and BPC molecules on different crystal planes of Zn.

attributed to the $–CF_2$ group of the OBS molecule, and the other at 685.20 eV, corresponding to ZnF_2. The formation of ZnF_2 signifies the *in-situ* generation of a protective passivation layer on the Zn electrode surface [23]. Notably, XPS measurements of the cycled Zn anode yield consistent results, demonstrating the stability of these species during operation (Fig. S4 in the ESM).

The impact of this hybrid adsorption layer was reflected in the electrode morphology. As shown in Figs. 1(d) and 1(e), the ZSO-immersed sample displayed a rough and uneven surface covered with numerous bulky corrosion products (~ 10 μm in diameter), whereas the ZBF-immersed sample exhibited a much smoother surface. The corresponding energy-dispersive X-ray spectroscopy (EDS) analysis further reveals that the relative sulfur element content derived from corrosion products (ZHS) on the ZBF-immersed sample (4.64 wt.%) was only 49.62% of that on the ZSO-immersed sample (Figs. S5 and S6 in the ESM), suggesting substantially less self-corrosion of the Zn electrode in the ZBF electrolyte than that in the ZSO electrolyte. Furthermore, a homogeneous distribution of Bi and F elements was observed across the surface of the ZBF-immersed sample (Fig. 1(f)), suggesting the uniform coverage achieved by the synergistic adsorption of OBS and BPC.

Beyond chemical adsorption, the additives undergo electrochemical transformations during cycling. As shown in Fig. 1(g), distinct diffraction peaks corresponding to metallic Bi (PDF#97-067-1289) emerged in the XRD pattern of Zn electrode after cycling in a Zn||Zn symmetric cell with ZBF electrolyte, indicating the electrochemical reduction of Bi^{3+} from BPC additive

to Bi^0 in the cycling process. The *in-situ* generated Bi^0 is proposed to serve as preferential nucleation sites for Zn deposition and can enhance the corrosion resistance of Zn electrode [33]. In addition, diffraction peaks assigned to ZnF_2 (PDF#97-018-4219) were also detected, suggesting the concurrent formation of ZnF_2 on the electrode surface [41]. Significantly, the formation of ZnF_2 on Zn electrode can improve interfacial Zn^{2+} conductivity [42, 43]. The reaction equation for the formation of Bi and ZnF_2 can be described as follows (Eqs. (1) and (2))

$$2Bi^{3+} + 3Zn \rightarrow 2Bi + 3Zn^{2+} \quad (1)$$

$$(C_{15}H_4F_{17}SO_4)^- + Zn^{2+} + 2e^- \rightarrow ZnF_2 + R - R' \quad (2)$$

where R and R' represent unspecified organic groups formed as decomposition products of the fluorinated sulfonate additive.

DFT simulations are performed to further explore the chemical adsorption of OBS and BPC molecules on Zn anode. As depicted in Fig. 1(h), it was found that both OBS and BPC molecules exhibit more negative adsorption energies on the Zn surface compared to H_2O molecules. Specifically, the adsorption energies of OBS molecules on the Zn (002), Zn (100), and Zn (101) planes are −0.25, −1.00, and −3.85 eV, respectively, whereas those of BPC molecules are −1.21, −3.04, and −4.20 eV, respectively. These results confirm that the adsorption of OBS and BPC molecules on the Zn electrode surface is thermodynamically more favorable than that of H_2O molecules in the ZBF electrolyte, leading to the formation of an adsorption layer enriched with Bi and F elements. This layer effectively shields the Zn anode from direct contact with free H_2O molecules, thereby inhibiting Zn dendrite growth and side reactions [39]. Additionally, the $-CF_2-$ rich cross-linked network, constructed by adsorbed OBS molecules on the Zn electrode surface, not only homogenizes the interfacial electric field distribution but also guides the 3D diffusion of Zn^{2+} [23, 39]. It is noteworthy that both OBS and BPC molecules exhibit similar adsorption trends on Zn, with the strongest binding on the (101) plane and the weakest on the (002) plane. Thus, these molecules preferentially accumulate on the (101) and (100) planes, forming a dense adsorption layer that directs subsequent Zn deposition. In the initial deposition stage, positively charged Bi^{3+} preferentially adsorb on the electrode protrusions, creating an electrostatic shielding effect that induces uniform Zn^{2+} nucleation [37]. Subsequently, these Bi^{3+} are reduced *in-situ* to form a metallic Bi layer. This zincophilic layer further guides the Zn^{2+} deposition on the Zn (002) plane and suppresses irreversible side reactions. Additionally, a ZnF_2-rich interface modulates the nucleation behavior of Zn^{2+}, promoting thermodynamically favorable Zn (002) plane deposition and thereby suppressing dendrite formation. This functional mechanism of ZnF_2 is considered beneficial for enhancing the cycling stability of Zn anodes, analogous to the role of the LiF/Li interface layer on lithium metal anodes [44, 45]. Therefore, the synergistic effect of interface modulation, including selective adsorption, electrostatic shielding, and induced nucleation, significantly promotes the preferential growth of the Zn (002) plane during electrodeposition, ultimately resulting in a dense and uniform Zn deposition layer.

The solvation structures of the ZBF and ZSO electrolytes were characterized by IR and Raman spectroscopy. No significant changes were observed in the responding characteristic peaks, indicating that the influence of OBS and BPC on the solvation structure of Zn^{2+} can be ignored in this study (Figs. S7 and S8 in the ESM).

In conclusion, the synergistic adsorption of OBS and BPC constructs a multifunctional interfacial layer on the Zn electrode. The adsorbed organic molecules form a hydrophobic barrier against water-induced side reactions, while the concurrently generated metallic Bi and ZnF_2 composite regulates Zn deposition and facilitates ion conduction. This multifunctional interface thus ensures highly reversible and stable Zn plating/stripping in aqueous electrolyte.

2.2 Modulation of Zn deposition kinetics via the adsorption layer and facilitated desolvation

Considering the structural and composition characteristics, this as-formed protective layer is expected to contribute to suppressing water-induced side reactions and guiding the uniform deposition of Zn. Potentiodynamic polarization measurements were conducted to evaluate the corrosion behavior of Zn electrode in different electrolytes, and the corresponding corrosion current density (i_{corr}) values were derived from Tafel extrapolation of the polarization curves shown in Fig. 2(a). The Zn electrode exhibited comparable corrosion potential (E_{corr}) in ZSO (−1.02 V vs. saturated calomel electrode (SCE)) and ZBF electrolytes (−1.01 V vs. SCE), while the i_{corr} in the ZBF electrolyte (4.53 $mA{\cdot}cm^{-2}$) was 56.4% lower than that in the ZSO electrolyte (10.38 $mA{\cdot}cm^{-2}$). After 7 days of immersion in ZSO and ZBF electrolytes, the Zn electrodes were subjected to the potentiodynamic polarization tests in the corresponding electrolytes. The sample immersed in the ZBF electrolyte sample showed a more positive E_{corr} (−0.98 V vs. SCE) and a lower i_{corr} (4.85 $mA{\cdot}cm^{-2}$) compared to the ZSO-immersed sample (Fig. S9 in the ESM). These results indicate that the co-addition of OBS and BPC additives can significantly suppress the corrosion of the Zn electrode in the electrolyte. This improved corrosion resistance was further corroborated by characterizing the corrosion products on the samples after 7 days of immersion via XRD measurement. The XRD patterns of both samples exhibited diffraction peaks corresponding to the corrosion product $Zn_4SO_4(OH)_4{\cdot}5H_2O$ (PDF#00-039-0688) (Fig. 2(b)). However, the ZHS peak intensities for the ZBF-immersed sample were significantly lower than those for the ZSO-immersed sample, indicating that composite additive could effectively inhibit self-corrosion. These results consistently demonstrate that the hybrid adsorption layer significantly suppresses Zn corrosion.

Beyond corrosion inhibition, the additives synergistically enhance the interfacial wettability, which is crucial for homogeneous ion flux. Contact angle measurements (Fig. 2(c)) show that the contact angles for the ZSO and ZBF electrolytes on the Zn electrodes were measured to be 92.5° and 34.7°, respectively. Notably, the individual introduction of OBS or BPC also improved wettability, with corresponding contact angles of 52.7° and 43.8° (Fig. S10 in the ESM). The intermediate wetting behavior underscores the synergistic enhancement of electrolyte wettability by OBS and BPC. This synergy stems from the following dual mechanisms. Firstly, as a nonionic surfactant, OBS contains hydrophilic sulfonate groups and hydrophobic perfluorinated chains. Upon dissolution, its sulfonate groups form hydrogen bonds with bulk water molecules, weakening the cohesive attraction within the electrolyte. Simultaneously, the hydrophobic perfluorinated chains migrate to and align at the electrolyte/air interface, thereby weakening the interactions between surface water

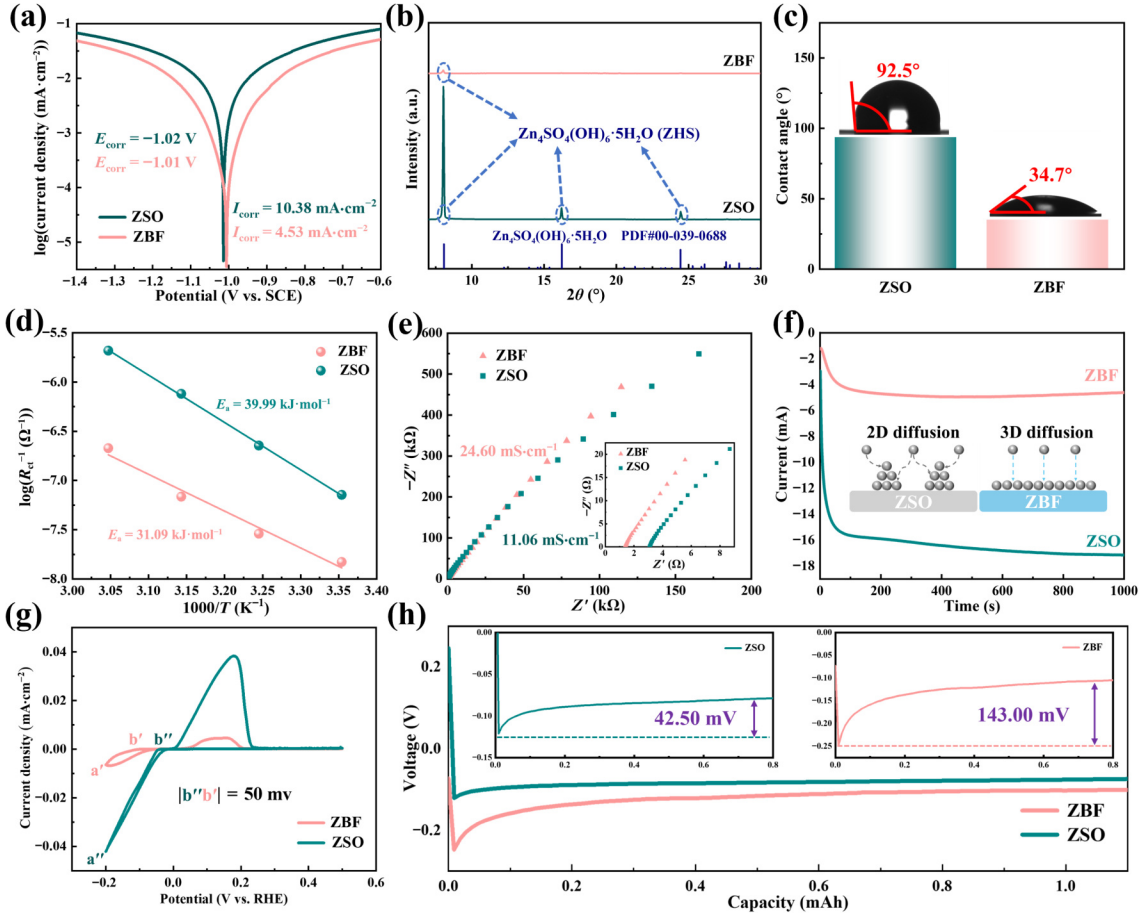

Figure 2 (a) Dynamic potential polarization curves of Zn electrodes in ZSO and ZBF electrolytes. (b) XRD patterns of Zn electrodes after 7 days immersion in ZSO and ZBF electrolytes. (c) Contact angles of ZSO and ZBF electrolytes on Zn electrodes. (d) Arrhenius curves and corresponding activation energies of Zn anodes in ZSO and ZBF electrolytes. (e) EIS spectra of SS||SS symmetric cells with ZSO and ZBF electrolytes. (f) Chronoamperograms of Zn||Zn symmetric cells with ZSO and ZBF electrolytes. (g) CV curves of Zn||SS asymmetric cells containing ZSO and ZBF electrolytes with a scanning rate of 1 mV·s^{-1}. (h) Voltage profile of the first plating process of the Zn||Cu asymmetric cell at 1 mA·cm^{-2}.

molecules. Secondly, citrate anions from BPC establish hydrogen bonds with water molecules in the bulk electrolyte, which reduces the attraction of these water molecules toward the surface. Consequently, the co-addition of OBS and BPC significantly lowers the surface tension of the electrolyte and enhances its wettability on the Zn electrode. Generally, the enhanced electrolyte wettability on the Zn electrode reduces electrode/electrolyte interfacial impedance, accelerating Zn^{2+} transport and improving charge transfer kinetics during Zn plating/stripping [46]. The improved wettability also homogenizes the interfacial current density distribution, thereby suppressing dendrite growth and side reactions [47].

The activation energy (E_a) for Zn^{2+} desolvation was determined by fitting the temperature dependence of the charge transfer resistance (R_{ct}) to the Arrhenius equation (Eq. (3)) [48]. The R_{ct} values were obtained from EIS measurements on Zn||Zn symmetric cells at temperatures of 25, 35, 45, and 55 °C (Fig. S11 in the ESM)

$$\frac{1}{R_{ct}} = A\exp\left(-\frac{E_a}{RT}\right) \quad (3)$$

where A is the prefactor, T is the thermodynamic temperature, and R is the gas constant. The calculated E_a for the Zn||Zn symmetrical cell in the ZBF electrolyte was 31.09 kJ·mol^{-1}, lower than that in ZSO electrolyte (39.99 kJ·mol^{-1}) (Fig. 2(d)). This reduced desolvation energy barrier indicates that the co-addition of OBS and BPC additives effectively facilitates the desolvation process by weakening the electrostatic interaction between Zn^{2+} and H_2O molecules. The ionic conductivity of the electrolytes was further evaluated through electrochemical impedance spectroscopy (EIS) measurements with stainless steel (SS)||SS symmetric cells. As shown in Fig. 2(e), the ZBF electrolyte exhibited an ionic conductivity of 24.60 mS·cm^{-1}, higher than that of the ZSO electrolyte (11.06 mS·cm^{-1}). This enhanced conductivity suggests improved Zn^{2+} mobility and more facile access to the electrode surface for electrochemical reactions. This finding further confirms that the hybrid adsorption layer facilitates the desolvation process, promoting the dissociation of Zn^{2+} from the solvation sheath formed by H_2O molecules.

The EIS measurements were conducted on Zn||Zn symmetric cells using Zn electrodes immersed in ZSO and ZBF electrolytes for three days (Fig. S12 in the ESM). The cell with ZBF-treated electrodes exhibited an ionic conductivity of 9.62 mS·cm^{-1} for Zn^{2+}, notably higher than that of the cell with ZSO-treated electrodes (8.27 mS·cm^{-1}). It is demonstrated that the ZnF_2 and Bi-based SEI form on the electrodes by the ZBF electrolyte, which enhances ionic conductivity, which facilitates rapid Zn^{2+} transport, reduces interfacial energy, and promotes uniform Zn^{2+} deposition.

To investigate the effect of additives on the Zn^{2+} diffusion kinetics during electrodeposition, chronoamperometry (CA) was employed

to measure transient current density in Zn||Zn symmetric cells using different electrolytes. As depicted in Fig. 2(f), the current density of the Zn anode persistently increased beyond 1000 s in ZSO electrolyte, indicating a non-uniform 2D diffusion process. During the planar diffusion process, the Zn^{2+} migration is driven by lateral concentration gradients and accumulates at local protrusions, promoting island nucleation and exacerbating the tip effect, which ultimately leads to the dendrite growth [49]. In contrast, in the ZBF electrolyte, the current density rapidly reached a quasi-steady-state plateau within ~ 100 s, reflecting that the mass transport process was dominated by stable 3D diffusion. Under this condition, the Zn^{2+} diffusion along the anode surface was constrained by the hybrid adsorption layer, and a time-invariant Zn^{2+} concentration gradient was maintained across the diffusion layer, thereby sustaining a steady Zn^{2+} diffusion flux from the bulk electrolyte toward the electrode surface [16]. This synergistic effect facilitated uniform Zn deposition and suppressed dendrite growth, ultimately yielding a smooth and dense Zn deposition layer.

The nucleation overpotential of Zn during plating process in the ZSO and ZBF electrolytes is tested by cyclic voltammetry (CV) tests in Zn||SS asymmetric cells. As shown in Fig. 2(g), the nucleation overpotential for Zn deposition in the ZBF electrolyte increased by approximately 50 mV relative to that in the ZSO electrolyte. Similarly, the voltage profiles of Zn||SS asymmetric cells displayed that the nucleation overpotential of Zn increased to 143.0 mV in the presence of OBS and BPC additives (Fig. 2(h)). According to the classical nucleation theory, the relationship between the size of electrodeposited Zn particles and the nucleation overpotential can be described by Eq. (4) [29]

$$r_{crit} = 2\frac{\gamma V_m}{F|\eta|} \quad (4)$$

where r_{crit} represents the critical radius of electrodeposited Zn particles, γ stands for the surface energy of electrode/electrolyte interface, V_m describes the molar volume of Zn, F is Faraday's constant, and η denotes the nucleation overpotential of Zn in the planting process. This relationship also suggests that a larger nucleation overpotential is beneficial for obtaining finer Zn particles during planting process. To the ZBF system, the increased overpotential can be attributed to the additional resistance introduced by the formation of adsorption layer and SEI, which reduces the nucleation rate via steric hindrance, resulting in the formation of a finer and denser Zn deposition layer [50].

The addition of OBS and BPC to the electrolyte enables their co-adsorption onto the Zn electrode surface, forming a H_2O-blocking functional adsorption layer that suppresses corrosion side reactions. Meanwhile, the additives improve the wettability of the electrolyte toward the Zn electrode, optimize Zn^{2+} transport kinetics, promote the desolvation process and uniform diffusion of Zn^{2+}, and collectively elevate the nucleation overpotential for Zn deposition, thereby guiding uniform Zn plating. The combined effects outlined above establish a stable electrode/electrolyte interface, providing a critical interfacial condition for AZIBs with long cycling lifespans.

2.3 Towards preferential (002) crystallographic orientation and dense Zn morphology

To reveal the effects of hybrid adsorption layer in promoting uniform Zn deposition, *in-situ* optical microscopy was employed to comparatively study the Zn plating behavior on the electrode in the baseline (ZSO) and modified (ZBF) electrolytes (Fig. 3(a)). In the ZSO electrolyte, uneven nucleation sites and protuberances emerged within 15 min of plating, which triggered a "tip effect" and grew continuously into dendrites during subsequent deposition. After 30 min, the Zn electrode was covered with many mossy Zn dendrites and protuberances. In contrast, the electrode in the ZBF electrolyte maintained a flat and homogeneous surface throughout the plating process. Even after 30 min, neither dendrites nor bubbles were observed, demonstrating that the ZBF electrolyte effectively inhibited Zn dendrite growth. The influence of the hybrid adsorption layer on the Zn deposition uniformity was further quantified by 3D optical profilometry (Fig. 3(b)). After 10 min of deposition at 1 $mA{\cdot}cm^{-2}$, the ZSO electrolyte produced irregular deposition with distinct dendrites, which could penetrate the separator and subsequently lead to a cell short circuit. Conversely, the ZBF electrolyte yielded a smooth and flat surface on the Zn electrode.

The influence of hybrid adsorption layer on the Zn deposition behavior was further investigated by XRD measurement, and the corresponding XRD patterns are shown in Fig. 3(c). After 20 h of cycling in the ZBF electrolyte, the diffraction peak intensity of Zn (002) plane was significantly lower than that of the Zn (101) plane. However, the peak intensity of Zn (002) plane increased progressively with prolonged cycling, indicating a strongly preferred (002) growth orientation. In contrast, the peak intensity of Zn (100) remained consistently low throughout the entire cycling process. To quantify the evolution of preferred orientation during Zn deposition, the intensity ratios of diffraction peaks (i.e., $R_1 = I_{(002)}/I_{(100)}$ and $R_2 = I_{(002)}/I_{(101)}$, where R_1 and R_2 are the intensity ratios of the (002)/(100) and (002)/(101) diffraction peaks, respectively, and $I_{(002)}$, $I_{(100)}$, and $I_{(101)}$ denote the diffraction peak intensities corresponding to the (002), (100), and (101) crystallographic planes, respectively) were taken as a reference index and the calculated values are presented in Fig. 3(e). Notably, in the ZBF electrolyte, R_1 and R_2 gradually increased from 0.47 and 0.12 (cycling for 20 h) to 2.22 and 0.54 after 600 h of cycling. The continuous increase in R_1 and R_2 confirms that Zn^{2+} preferentially deposited on the planar Zn (002) plane, leading to its dominant growth, which demonstrates the efficacy of the hybrid adsorption layer in templating (002)-oriented growth. Additionally, the diffraction peak intensity at 7.66° corresponding to ZHS by-products was obviously lower in the ZBF electrolyte than in the ZSO electrolyte after cycling, suggesting that by-product formation was substantially suppressed in the ZBF electrolyte.

The morphology of the Zn deposition layer in Zn||Zn symmetric cells was characterized by scanning electron microscopy (SEM). In the ZSO electrolyte, coarse dendrites grew on the anode after 50 h of cycling, ascribing to the uneven deposition of Zn and side reactions at the electrolyte/electrode interface (Fig. S13 in the ESM). However, as shown in Fig. 3(d), in the ZBF electrolyte, the anode surface exhibited a dense and flat appearance after 20 h of cycling. As cycling proceeded, a uniform deposited layer composed of closely packed hexagonal grains was formed on the anode surface, originating from the compact stacking of Zn (002) planes normal to the electrode surface [51]. The formation of this well-oriented texture can be attributed to synergistic functions within the adsorption layer. Firstly, the molecular adsorption component (from OBS/BPC) modulates the interfacial Zn^{2+} flux and desolvation kinetics, promoting uniform ion distribution at the electrode/electrolyte interface. Secondly, in the electrodeposition

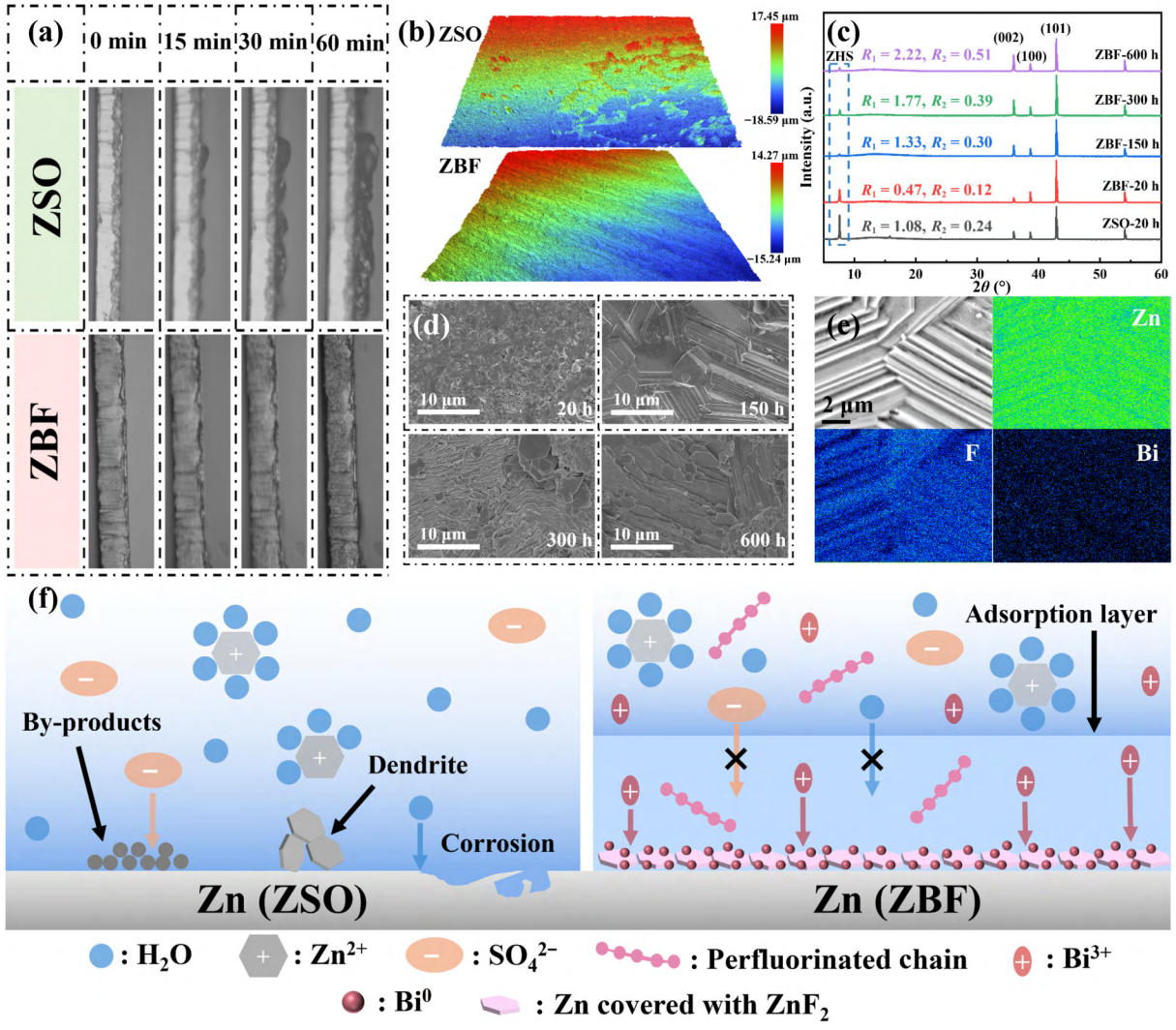

Figure 3 (a) *In-situ* optical microscopy images of Zn deposition in ZSO and ZBF electrolytes. (b) 3D morphology of Zn deposition layers in ZSO and ZBF electrolytes. (c) XRD patterns of Zn anode cycled in ZBF electrolyte for different times and (d) corresponding surface morphology. (e) EPMA elemental maps of the Zn electrode surface after 7 days of immersion in ZBF electrolyte. (f) Schematic representation of the Zn deposition process in ZSO and ZBF electrolyte.

process, the reduced metallic Bi on the electrode surface provides abundant zincophilic nucleation sites, while the ZnF_2 facilitates interfacial ion transport and stabilizes the electrode surface. More critically, the preferential growth of these Zn (002) planes effectively suppresses the formation and growth of dendrites, while also mitigating the side reactions and thereby reducing the generation of by-products [52].

The spatial homogeneity and durability of this hybrid protective layer were evaluated by electron probe X-ray micro analyzer (EPMA). As shown in Fig. 3(e) and Fig. S14 in the ESM, uniformly distributed F and Bi signals were maintained on both the immersed and cycled Zn electrodes. More importantly, the cycled electrode exhibited a denser Zn deposition layer with more pronounced preferred growth along (002) crystal plane compared to the immersed electrode. This denser and highly oriented morphology originated from a more uniform electrodeposition process under the applied electric field, enabled by the homogeneous Bi/ZnF_2-modified interface. The near-identical characteristic X-ray intensities (Fig. S15 in the ESM) demonstrate that the atomic surface content of F and Bi is almost unchanged after cycling compared to the initial immersion state. These findings confirm that the initially formed interphases (metallic Bi and ZnF_2) not only possess chemical stability but also maintain their spatial homogeneity throughout long-term electrochemical cycling. This retention ensures the persistent regulatory functions of the hybrid adsorption layer throughout cycling, which is fundamental to achieving long-term stability of AZIBs.

Based on the results, the evolution of Zn deposition is decisively regulated by the hybrid adsorption layer. This layer integrates the functions of molecular adsorption and a stable inorganic/organic interfacial phase to coordinate nucleation, homogenize ion transport, and induce preferential crystallographic growth. But more importantly, it can induce Zn to grow preferentially along the (002) crystal plane. Collectively, these effects suppress dendritic formation and mitigate side reactions, resulting in a compact and homogeneous Zn deposition layer. The contrasting deposition behaviors with and without this regulatory layer are schematically illustrated in Fig. 3(f).

2.4 Highly reversible Zn plating/stripping

To evaluate the impact of electrolytes on the cycling stability of Zn||Zn symmetric cells, the galvanostatic cycling tests were

conducted at different current densities and areal capacities. The cell with ZSO electrolyte exhibited significant voltage fluctuations after cycling for 150 h in the condition of 1 mA·cm^{-2} and 1 mAh·cm^{-2}, which can be attributed to the short internal soft circuit induced by Zn dendrite growth (Fig. 4(a)). To the ZBF electrolyte system, the cell maintains stable cycling for over 6600 h (> 9 months), representing a 44-fold longer cycling lifespan compared to the ZSO-based cell. Although the individual addition of OBS or BPC to the ZSO electrolyte moderately improved the cycling lifespan of Zn||Zn symmetric cells (Fig. S16 in the ESM), both systems exhibited markedly inferior performance relative to that of the ZBF electrolyte system, delivering less than half of the cycle life of the ZBF-based cell. Even when the current density and areal capacity increased to 3 mA·cm^{-2} and 3 mAh·cm^{-2}, the Zn||Zn symmetric cell with ZBF electrolyte still works stably over 1000 h (Fig. 4(b)). On the other hand, the Zn||Zn symmetric cell with ZSO electrolyte rapidly failed after only 70 h and underperformed relative to that of Zn||Zn batteries with electrolytes modified with individual OBS or BPC additives (Fig. S17 in the ESM). The significant improvement in battery cycle performance is attributed to the fact that OBS facilitates the formation of a ZnF_2 interface that suppresses side reactions and homogenizes Zn^{2+} flux, while Bi acts as a nucleation site to guide preferential (002) deposition.

The rate performance of Zn||Zn symmetric cells was evaluated over a current density range of 0.5–7 mA·cm^{-2} to assess the Zn plating/stripping efficiency. As shown in Fig. 4(c), an internal short circuit occurred in the cell with the ZSO electrolyte when the current density increased to 5 mA·cm^{-2}. However, to the ZBF electrolyte system, the cell exhibited reversible Zn plating/stripping even up to 7 mA·cm^{-2} and still maintained stable operation when the current density was restored to 0.5 mA·cm^{-2}. Additionally, the reversibility of Zn plating/stripping in different electrolyte systems was further assessed via CE measurements performed on Zn||Cu asymmetric cells. As shown in Fig. 4(d) and Fig. S18 in the ESM, the cell in the ZSO electrolyte experienced rapid failure due to irreversible side reactions as well as dendritic growth, ceasing operation after only 170 cycles at 1 mA·cm^{-2} and 1 mAh·cm^{-2}. In comparison, the incorporation of both OBS and BPC into the electrolyte significantly extended the cycling lifespan of the Zn||Cu asymmetric cells. Notably, the cell sustained up to 1000 cycles with a CE reaching 99.8%. Even at the current density of 3 mA·cm^{-2} (Fig. S19 in the ESM), the cell with ZBF electrolyte delivered an average CE of 99.71% over 450 cycles, whereas the cell with ZSO electrolyte failed after 100 cycles, despite showing an average CE of 99.90%. These results highlight the substantial improvement in rate performance afforded by incorporating both OBS and BPC into the electrolyte, which exceeds the performance limits of the conventional ZSO electrolyte.

To understand the underlying mechanism, morphology analysis was performed on Zn electrodes from Zn||Cu asymmetric cells after 50 cycles at 1 mA·cm^{-2} and 1 mAh·cm^{-2} in different electrolytes (Fig. S20 in the ESM). In the ZSO system, both electrodes showed porous and loosely packed Zn deposition. In contrast, the Zn electrode in the ZBF system exhibited a dense and uniform deposition layer oriented along the Zn (002) planes. Moreover, the deposition layer on the Cu electrode featured a closely packed submicron-sized Zn grain. These morphological characteristics demonstrate that the synergistic effect of OBS and BPC additives in the electrolyte directs the preferential lateral growth of the Zn deposition layer along the electrode surface, ultimately leading to a compact and uniform structure. This optimization effectively suppresses the Zn dendrite growth and reduces the irreversible electrolyte consumption during plating/stripping cycles, thus contributing to the superior rate performance of the ZBF electrolyte system.

To assess the interfacial cycling stability, Zn||Zn symmetric cells with different electrolytes were examined by *ex-situ* EIS (Figs. S21 and S22 in the ESM), using the equivalent circuit model shown in the inset of Fig. S19 in the ESM for data fitting. The initial R_{ct} of the ZBF-based cell was 4965 Ω, which was higher than that of the ZSO-based cell (2318 Ω). This elevated R_{ct} resulted from the strong steric hindrance effect caused by OBS and BPC as adsorbed species on the Zn electrode [50]. However, the R_{ct} of the ZBF-based cell decreased during the initial stages of cycling and then stabilized around 329.5 Ω after 200 h of operation.

To gain mechanistic insights into the evolution of Zn electrodeposition, distribution of relaxation times (DRT) analyses were conducted on the EIS data for ZSO and ZBF electrolyte systems. This method effectively decouples the interfacial kinetics influenced by substrate chemistry [53]. The DRT curves (Fig. S23 in the ESM) yielded five relaxation time constants (τ, in seconds): τ_1 = 2.33 × 10^{-5} s (associated with the electrode/electrolyte interface impedance (R_{SEI})), τ_2 = 1.86 × 10^{-3} s (fast Zn^{2+} adsorption forming the electric double layer (R_{ad})), τ_3 = 1.46 × 10^{-2} s (Zn^{2+} migration at the electrode surface (R_{mig})), τ_4 = 0.11 s (charge‑transfer impedance (R_{ct})), and τ_5 = 0.96 s (Zn^{2+} diffusion in the electrolyte (R_{diffu})) [54]. As shown in Fig. S24 in the ESM, upon extending the deposition time from 0 to 400 s at 10 mA·cm^{-2}, the R_{ct} in both systems exhibits an initial gradual decline followed by stabilization. Specifically, the R_{ct} of the ZBF electrolyte system stabilizes more rapidly. As shown in Figs. 4(f) and 4(g), the peaks exhibit a progressive decrease in both impedance magnitude and relaxation time during Zn plating, indicating accelerated interfacial kinetics. Notably, the ZBF electrolyte system exhibits faster charge transfer kinetics, more rapid Zn^{2+} migration across the electrode surface, and enhanced Zn^{2+} diffusion within the electrolyte.

Building upon these demonstrated improvements in cycling lifespan, rate capability, and controlled deposition morphology, the overall performance was benchmarked against recent high-performing systems. As summarized in Fig. 4(e) and Table S1 in the ESM, the ZBF-based cell exhibits highly competitive performance in terms of current density, areal capacity, and cycling lifespan when compared with several recently reported systems [55–63]. These results collectively highlight that co-addition of OBS and BPC is a promising strategy for enhancing AZIBs.

2.5 Electrochemical performance of Zn||Mg^{2+}-modified $NH_4V_4O_{10}$ (denoted as MNVO) full cells

To evaluate the efficacy of ZBF electrolyte in augmenting the overall performance of batteries, MNVO was employed as the cathode material to assemble full cells. The XRD pattern (Fig. S25 in the ESM) closely matched International Center for Diffraction Data (ICDD) PDF card (PDF#01-089-2485) for $NH_4V_4O_{10}$, indicating the successful synthesis of the MNVO material. Additionally, the SEM image (Fig. S26 in the ESM) reveals a flower-shaped morphology and uniform elemental distribution of the synthesized MNVO, which are consistent with the previous report [64].

Figure 5(a) schematically illustrates the working mechanism of Zn||MNVO full cells. The CV curves, obtained at a scan rate of 1 mV·s^{-1}, reveal the same multiple pairs of oxidation and reduction

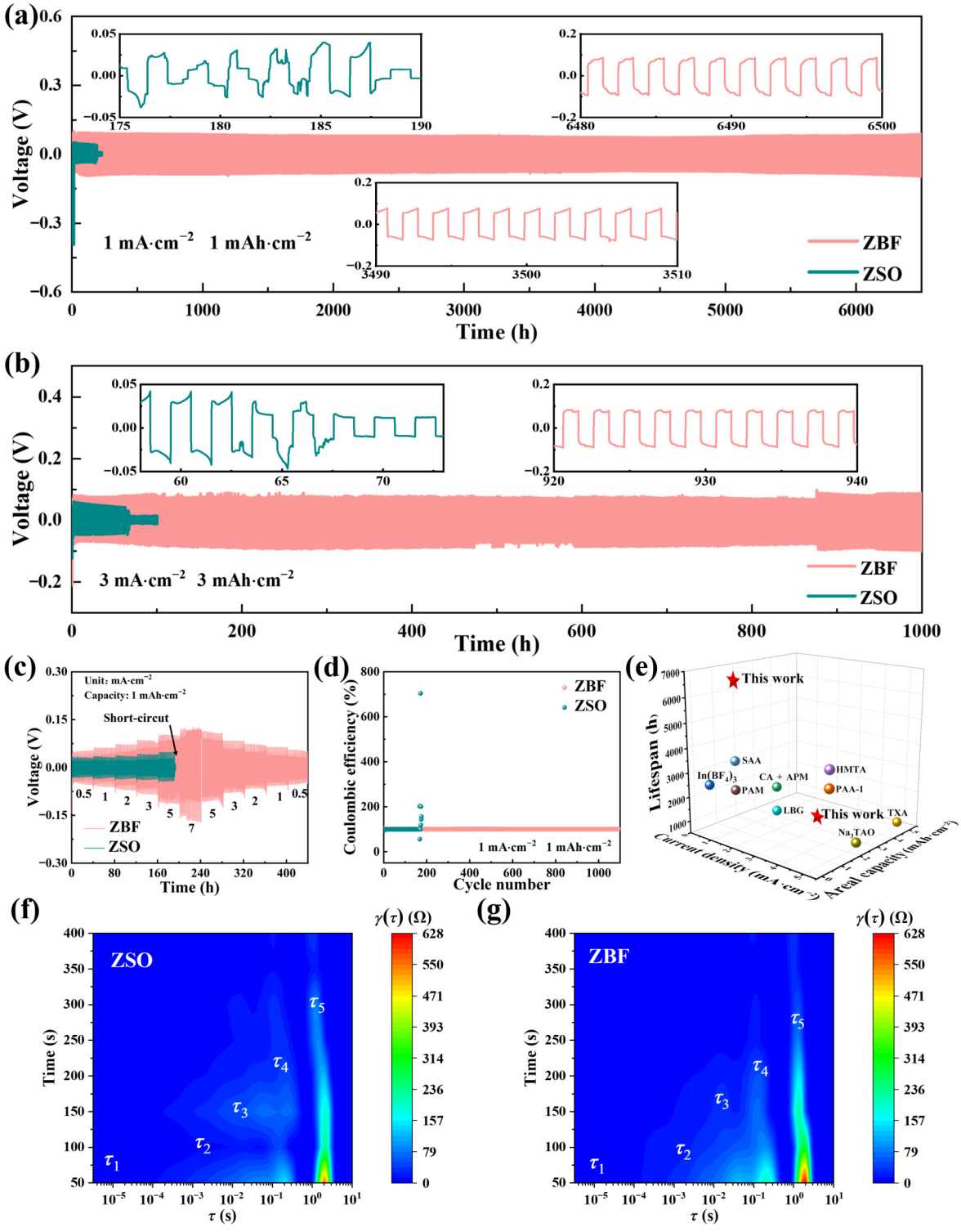

Figure 4 (a) Cycling performance of Zn||Zn symmetric cell at 1 mA·cm^{-2} and 1 mAh·cm^{-2}. (b) Cycling performance of Zn||Zn symmetric cell at 3 mA·cm^{-2} and 3 mAh·cm^{-2}. (c) Rate performance of Zn||Zn symmetric cell. (d) Coulombic efficiency of Zn||Cu asymmetric cell at 1 mA·cm^{-2} and 1 mAh·cm^{-2}. (e) Long-term cycling performance of Zn||Zn symmetric cell with ZBF electrolyte against previously reported systems. The DRT contour plots during the Zn deposition process on (f) ZSO and (g) ZBF at a current density of 10 mA·cm^{-2}.

peaks for cells employing both electrolytes, indicating the Zn^{2+} insertion and extraction processes in the MNVO lattice (Fig. 5(b)). Moreover, there is no significant difference in the shape of the two curves of the Zn||MNVO full cells with/without co-additives of OBS and BPC, that is, the negligible influence of these additives on the redox reactions of MNVO in the charging/discharging process. However, the CV curve of the Zn||MNVO full cells in the ZBF electrolyte exhibits a smaller difference between the oxidation and reduction peaks compared to the ZSO electrolyte, suggesting reduced voltage polarization. This improvement is attributed to the

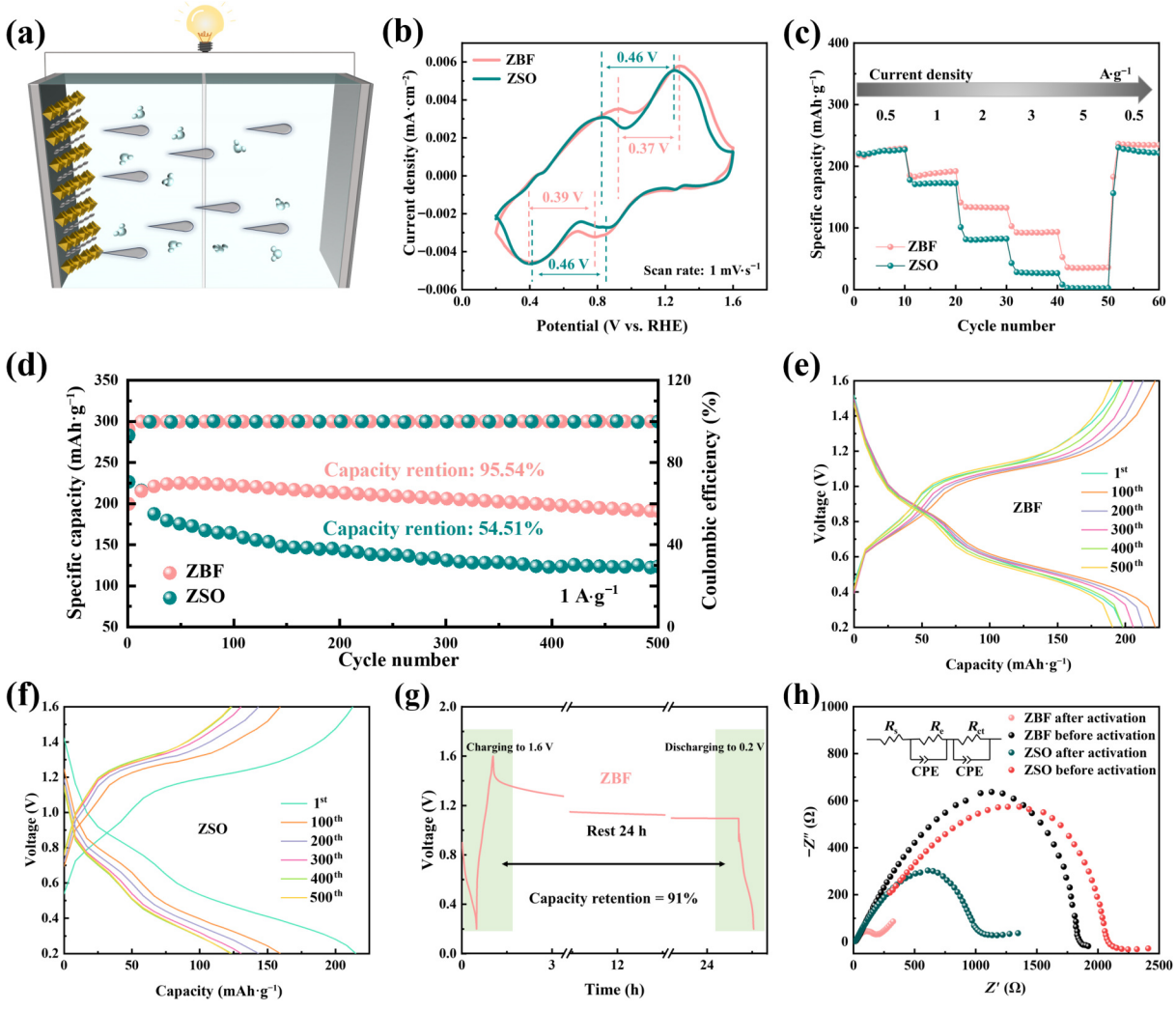

Figure 5 (a) Schematic diagram of the Zn||MNVO full cells. (b) CV curves of Zn||MNVO full cells at a scan rate of 1 mV·s^{-1}. (c) Rate performance of the Zn||MNVO full cells at different current densities. (d) Cycling performance of Zn||MNVO full cells at a current density of 1 A·g^{-1}. Charge–discharge curves of the Zn||MNVO full cells with ZBF (e) and ZSO (f) electrolytes. (g) Capacity retention of the Zn||MNVO full cell with ZBF electrolyte. (h) EIS spectra of the Zn||MNVO full cells with ZSO and ZBF electrolytes before and after activation.

accelerated charge transfer and Zn^{2+} storage kinetics resulting from the co-addition of OBS and BPC additives. The rate performance of Zn||MNVO full cells with different electrolytes was shown in Fig. 5(c). The specific capacity of cells with ZBF electrolyte was 229.32, 192.04, 133.67, 96.27, and 35.12 mAh·g^{-1}, respectively, under the current density of 0.5–5 A·g^{-1}. At each current density, the specific capacity of the cell with ZBF electrolyte was higher than that of the cell with ZSO electrolyte [27].

The advantages of ZBF electrolyte toward the Zn||MNVO full cells are further validated by the superior capacity retention during prolonged cycling at 1 A·g^{-1} (Fig. 5(d)). The cell with ZBF electrolyte delivered a higher discharge capacity of 190.8 mAh·g^{-1} with a capacity retention of 95.5% after 500 cycles, and its maximum achieved capacity was 199.7 mAh·g^{-1}. In contrast, the cell with ZSO electrolyte retained only 54.5% of its capacity under the same conditions. The corresponding charge–discharge profiles (Figs. 5(e) and 5(f)) reveal that the ZBF-based cell experienced a minimal increase in polarization during cycling, whereas the ZSO-based cell suffered a substantial increase, highlighting the superior compatibility between the ZBF electrolyte and the MNVO cathode. Furthermore, the Zn||MNVO full cell with the ZBF electrolyte exhibits desirable electrochemical performance, even at high current density (3 A·g^{-1}) (Fig. S27 in the ESM). Additionally, the self-discharge performance in various electrolytes was evaluated to assess the durability of full cells. As shown in Fig. 5(g), the full cell utilizing ZBF electrolyte retained an impressive 91% of its initial discharge capacity. This performance surpasses the cell employing ZSO electrolyte, which remained only 86% under the same conditions (Fig. S28 in the ESM). To gain further insight into the underlying mechanisms, the cycled Zn anodes were examined by XRD and SEM measurements. The XRD patterns of the Zn anode cycled in ZSO electrolyte (Fig. S29 in the ESM) show distinct diffraction peaks of ZHS by-products, indicating severe side reactions. Furthermore, SEM images (Fig. S30 in the ESM) reveal disordered deposits and large lumpy protrusions on the Zn anode cycled in ZSO electrolyte, whereas the anode cycled in ZBF electrolyte remains flat and dendrite-free. The interfacial stability of the full cells was further evaluated by EIS measurements (Fig. 5(h)). The R_{ct} of the full cell with the ZSO electrolyte remained as high as 1544 Ω after activation, approximately one order of magnitude larger than that of the ZBF-based system. By contrast, the R_{ct} of the full cell with the ZBF electrolyte decreased significantly from an initial value of 641.3 to 89.4 Ω after activation. This notable

reduction indicates an optimized Zn anode/electrolyte interface, where side reactions are effectively suppressed, leading to a lower interfacial resistance. In summary, these results indicate that the ZBF electrolyte enhances charge transfer and facilitates Zn^{2+} desolvation, promotes oriented Zn (002) deposition, and suppresses by-product formation, thereby improving the overall electrochemical performance of the full cell.

3 Conclusions

In summary, this study proposes a rational electrolyte design strategy for AZIBs by introducing trace amounts of OBS and BPC additives. This approach enables the *in-situ* construction of a multifunctional hybrid interphase on the Zn anode, which fundamentally stabilizes the electrode/electrolyte interface. This mechanically stable interface is composed of organic adsorption layer and inorganic components (metallic Bi and ZnF_2). The former protects Zn anode from infringement of water molecules, while the latter assists in homogenizing zinc ion flux and guiding the planar growth of zinc along the basal Zn (002) plane. Consequently, the Zn||Zn symmetric cell achieves an exceptional cycling lifespan over 6600 h at 1 $mA·cm^{-2}$ and 1 $mAh·cm^{-2}$, and the Zn||MNVO full cell retains 95.54% of discharge capacity after 500 cycles at 1 $A·g^{-1}$. This work underscores the efficacy of constructing the multifunctional hybrid interphase through synergistic dual-additive strategy, offering a promising and scalable pathway toward durable and high-performance AZIBs.

Electronic Supplementary Material: Supplementary material (details of experimental section; Figs. S1–S30: EDL test curves, calculated energy levels, XPS spectrum, SEM images, EDS spectrum, XRD patterns, contact angle, alternating current (AC) impedance test curves, the activation energy test curves, ionic conductivities, DRT plots, charge and then discharge curves of the full cells, FTIR spectra, Raman spectra, long-term cycling performance; and Table S1) is available in the online version of this article at https://doi.org/10.26599/NR.2026.94908690.

Data availability

All data needed to support the conclusions in the paper are presented in the manuscript and the Electronic Supplementary Material. Additional data related to this paper may be requested from the corresponding author upon request.

Acknowledgements

This work was supported by the Innovation Fund of Postgraduate, Sichuan University of Science & Engineering (No. Y2024055); Leshan West Silicon Materials Photovoltaic New Energy Industry Technology Research Institute (No. 2023GY11); Key Laboratory of Materials and Surface Technology, Ministry of Education (No. xxx-2024-yb009); the Sichuan Science and Technology Program (No. 2024NSFSC0955); and the Opening Project of Material Corrosion and Protection Key Laboratory of Sichuan Province (No. 2017CL04).

Declaration of competing interest

All the contributing authors report no conflict of interests in this work.

Author contribution statement

L. X.: Experimental design, data curation, formal analysis, funding acquisition, writing – original draft. H. L.: Project administration, supervision, funding acquisition. Y. L.: Experimental design, funding acquisition, supervision, writing – review & editing. Y. G.: Supervision, funding acquisition, writing – review & editing. All the authors have approved the final manuscript.

Use of AI statement

None.

References

[1] Li, Y.; Zhang, J. W.; Chen, Q. G.; Xia, X. H.; Chen, M. H. Emerging of heterostructure materials in energy storage: A Review. *Adv. Mater.* **2021**, *33*, 2100855.

[2] He, P.; Yan, M. Y.; Zhang, G. B.; Sun, R. M.; Chen, L. N.; An, Q. Y.; Mai, L. Layered VS_2 nanosheet-based aqueous Zn ion battery cathode. *Adv. Energy Mater.* **2017**, *7*, 1601920.

[3] Li, Q.; Zhao, Y. W.; Mo, F. N.; Wang, D. H.; Yang, Q.; Huang, Z. D.; Liang, G. J.; Chen, A.; Zhi, C. Y. Dendrites issues and advances in Zn anode for aqueous rechargeable Zn-based batteries. *EcoMat* **2020**, *2*, e12035.

[4] Lv, Y. Q.; Zhao, M.; Du, Y. D.; Kang, Y.; Xiao, Y.; Chen, S. M. Engineering a self-adaptive electric double layer on both electrodes for high-performance zinc metal batteries. *Energy Environ. Sci.* **2022**, *15*, 4748–4760.

[5] He, H. B.; Qin, H. Y.; Wu, J.; Chen, X. F.; Huang, R. S.; Shen, F.; Wu, Z. R.; Chen, G. N.; Yin, S. B.; Liu, J. Engineering interfacial layers to enable Zn metal anodes for aqueous zinc-ion batteries. *Energy Storage Mater.* **2021**, *43*, 317–336.

[6] Liu, S. L.; Zhang, R. Z.; Mao, J. F.; Zhao, Y. L.; Cai, Q.; Guo, Z. P. From room temperature to harsh temperature applications: Fundamentals and perspectives on electrolytes in zinc metal batteries. *Sci. Adv.* **2022**, *8*, eabn5097.

[7] Wang, S. B.; Ran, Q.; Yao, R. Q.; Shi, H.; Wen, Z.; Zhao, M.; Lang, X. Y.; Jiang, Q. Lamella-nanostructured eutectic zinc-aluminum alloys as reversible and dendrite-free anodes for aqueous rechargeable batteries. *Nat. Commun.* **2020**, *11*, 1634.

[8] Ren, Q. Q.; Tang, X. Y.; Guo, Y. Q.; Liao, X. B.; Zhang, C. M.; Zhu, Z. X.; Wang, P. P.; Wang, W.; Li, Y.; Song, W. J. et al. Achieving the dendrite-free Zn anode by inducing the (101)-preferred electrodeposition of Zn crystals. *Adv. Energy Mater.* **2025**, *15*, 2403961.

[9] Zeng, Y. X.; Zhang, X. Y.; Qin, R. F.; Liu, X. Q.; Fang, P. P.; Zheng, D. Z.; Tong, Y. X.; Lu, X. H. Dendrite-free zinc deposition induced by multifunctional CNT frameworks for stable flexible Zn-ion batteries. *Advi. Mater.* **2019**, *31*, 1903675.

[10] Li, Q. X.; Cui, X. M.; Pan, Q. M. Self-healable hydrogel electrolyte toward high-performance and reliable quasi-solid-state Zn–MnO_2 batteries. *ACS Appl. Mater. Interfaces* **2019**, *11*, 38762–38770.

[11] Jiang, R. H.; Naren, T.; Chen, Y. J.; Chen, Z.; Zhang, C. X.; Xie, Y. M.; Chen, L. B.; Qi, Y. Y.; Meng, Q. F.; Wei, W. F. et al. Enhanced hydrogen bonding through strong water-locking additives for long-term cycling of zinc-ion batteries. *Adv. Funct. Mater.* **2024**, *34*, 2411477.

[12] Khan, Z.; Kumar, D.; Crispin, X. Does water-in-salt electrolyte subdue issues of Zn batteries. *Adv. Mater.* **2023**, *35*, 2300369.

[13] Zhang, N.; Chen, X. Y.; Yu, M.; Niu, Z. Q.; Cheng, F. Y.; Chen, J. Materials chemistry for rechargeable zinc-ion batteries. *Chem. Soc. Rev.* **2020**, *49*, 4203–4219.

[14] Bayaguud, A.; Luo, X.; Fu, Y. P.; Zhu, C. B. Cationic surfactant-type

electrolyte additive enables three-dimensional dendrite-free zinc anode for stable zinc-ion batteries. *ACS Energy Lett.* **2020**, *5*, 3012–3020.

[15] Chen, N.; Huang, Y.; Lv, Y.; Wang, W. J. The effect of sodium dodecyl sulphate additives on the electrochemical performance of aqueous zinc-ion batteries. *Molecules* **2025**, *30*, 529.

[16] Xie, W. L.; Zhu, K. Y.; Jiang, W. K.; Yang, H. M.; Ma, M. X.; Zhao, L. L.; Yang, W. S. Highly 002-oriented dendrite-free anode achieved by enhanced interfacial electrostatic adsorption for aqueous zinc-ion batteries. *ACS Nano* **2024**, *18*, 21184–21197.

[17] Li, Y. H.; Wu, P. F.; Zhong, W.; Xie, C. L.; Xie, Y. L.; Zhang, Q.; Sun, D.; Tang, Y. G.; Wang, H. Y. A progressive nucleation mechanism enables stable zinc stripping-plating behavior. *Energy Environ. Sci.* **2021**, *14*, 5563–5571.

[18] Ding, Y. Q.; Zhang, X. T.; Wang, T. Q.; Lu, B. A.; Zeng, Z. Y.; Tang, Y.; Zhou, J.; Liang, S. Q. A dynamic electrostatic shielding layer toward highly reversible Zn metal anode. *Energy Storage Mater.* **2023**, *62*, 102949.

[19] Zhao, R. R.; Wang, H. F.; Du, H. R.; Yang, Y.; Gao, Z. H.; Qie, L.; Huang, Y. H. Lanthanum nitrate as aqueous electrolyte additive for favourable zinc metal electrodeposition. *Nat. Commun.* **2022**, *13*, 3252.

[20] Guo, Y. H.; Jia, Y. Y.; Wang, S.; Wang, L.; Liu, S. A rechargeable aqueous dendrite-free zinc-ion battery with robust performance enabled by the design of electrolyte additive. *J. Power Sources* **2025**, *642*, 236981.

[21] Cao, J. H.; Zhao, F.; Guan, W. X.; Yang, X. X.; Zhao, Q. D.; Gao, L. G.; Ren, X. F.; Wu, G.; Liu, A. M. Additives for aqueous zinc-ion batteries: Recent progress, mechanism analysis, and future perspectives. *Small* **2024**, *20*, 2400221.

[22] Geng, Y. F.; Pan, L.; Peng, Z. Y.; Sun, Z. F.; Lin, H. C.; Mao, C. W.; Wang, L.; Dai, L.; Liu, H. D.; Pan, K. M. et al. Electrolyte additive engineering for aqueous Zn ion batteries. *Energy Storage Mater.* **2022**, *51*, 733–755.

[23] Xu, W. W.; Li, J. T.; Liao, X. B.; Zhang, L.; Zhang, X. M.; Liu, C. Z.; Amine, K.; Zhao, K. N.; Lu, J. Fluoride-rich, organic–inorganic gradient interphase enabled by sacrificial solvation shells for reversible zinc metal batteries. *J. Am. Chem. Soc.* **2023**, *145*, 22456–22465.

[24] Huang, J. X.; Fu, Z.; Sun, C. F.; Deng, W. Z. Surfactant additives containing hydrophobic fluorocarbon chains and hydrophilic sulfonate anion for highly reversible Zn anode. *Molecules* **2023**, *28*, 4177.

[25] Shen, C.; Zhang, Y. X.; Li, X.; Guo, P.; Zeng, X.; Ni, K. Q.; Cao, R. F.; Wang, Z. G.; Wang, Z. L.; Qin, L. A multifunctional ionic liquid additive providing a solvation structure and electrostatic shielding layer for highly stable aqueous zinc-ion batteries. *J. Mater. Chem. A* **2025**, *13*, 2174–2186.

[26] Liu, Z. J.; Xi, M. R.; Sheng, R.; Huang, Y. D.; Ding, J.; Tan, Z. L.; Li, J. P.; Zhang, W. J.; Wang, Y. G. Zn(TFSI)$_2$-mediated ring-opening polymerization for electrolyte engineering toward stable aqueous zinc metal batteries. *Nano-Micro Lett.* **2025**, *17*, 120.

[27] Wu, Y.; Zhu, Z. H.; Shen, D.; Chen, L. N.; Song, T. Y.; Kang, T. X.; Tong, Z. Q.; Tang, Y. B.; Wang, H.; Lee, C. S. Electrolyte engineering enables stable Zn-ion deposition for long-cycling life aqueous Zn-ion batteries. *Energy Storage Mater.* **2022**, *45*, 1084–1091.

[28] Wang, L. Q.; Zhao, Z. D.; Yao, Y.; Zhang, Y. X.; Meng, Y. H.; Hu, B.; Kang, J. M.; Guo, J.; Zhang, L.; Lu, H. B. Highly fluorinated non-aqueous solid–liquid hybrid interface realizes water impermeability for anti-calendar aging zinc metal batteries. *Energy Storage Mater.* **2023**, *62*, 102920.

[29] Zhao, F. J.; Jing, Z. F.; Guo, X. X.; Li, J. W.; Dong, H. B.; Tan, Y. S.; Liu, L. X.; Zhou, Y. Q.; Owen, R.; Shearing, P. R. et al. Trace amounts of fluorinated surfactant additives enable high performance zinc-ion batteries. *Energy Storage Mater.* **2022**, *53*, 638–645.

[30] Guo, X.; Hong, H.; Li, Q.; Zhu, J. X.; Wu, Z. X.; Wang, Y. B.; Yang, S.; Huang, Z. D.; Huang, Y.; Li, N. et al. Dual robust electrode–electrolyte interfaces enabled by fluorinated electrolyte for high-performance zinc metal batteries. *Matter* **2024**, *7*, 4014–4030.

[31] Chen, R. W.; Zhang, C. Y.; Li, J. W.; Du, Z. J.; Guo, F.; Zhang, W.; Dai, Y. H.; Zong, W.; Gao, X.; Zhu, J. X. et al. A hydrated deep eutectic electrolyte with finely-tuned solvation chemistry for high-performance zinc-ion batteries. *Energy Environ. Sci.* **2023**, *16*, 2540–2549.

[32] Wang, M. M.; Meng, Y. H.; Chen, N.; Chuai, M. Y.; Shen, C. Y.; Zheng, X. H.; Yuan, Y.; Sun, J. F.; Xu, Y.; Chen, W. Electrolyte regulation of bismuth ions toward high-performance aqueous manganese-based batteries. *ACS Mater. Lett.* **2021**, *3*, 1558–1565.

[33] Zhao, R. Z.; Dong, X. S.; Liang, P.; Li, H. P.; Zhang, T. S.; Zhou, W. H.; Wang, B. Y.; Yang, Z. D.; Wang, X.; Wang, L. P. et al. Prioritizing hetero-metallic interfaces via thermodynamics inertia and kinetics zincophilia metrics for tough Zn-based aqueous batteries. *Adv. Mater.* **2023**, *35*, 2209288.

[34] Zhao, Y. M.; Du, A. B.; Dong, S. M.; Jiang, F.; Guo, Z. Y.; Ge, X. S.; Qu, X. L.; Zhou, X. H.; Cui, G. L. A bismuth-based protective layer for magnesium metal anode in noncorrosive electrolytes. *ACS Energy Lett.* **2021**, *6*, 2594–2601.

[35] Sui, Y. M.; Ji, X. L. Anticatalytic strategies to suppress water electrolysis in aqueous batteries. *Chem. Rev.* **2021**, *121*, 6654–6695.

[36] Guo, W. Q.; Yan, S. X.; Wang, S. Y.; Jing, L.; Mao, C. M.; Zhang, Z. H.; Peng, H. R.; Guo, X. S.; Li, G. C. A simple route to fabricate an artificial interface protective layer on a Zn anode for aqueous Zn-ion batteries. *ChemistrySelect* **2022**, *7*, e202200926.

[37] Wang, M. M.; Meng, Y. H.; Li, K.; Ahmad, T.; Chen, N.; Xu, Y.; Sun, J. F.; Chuai, M.; Zheng, X. H.; Yuan, Y. et al. Toward dendrite-free and anti-corrosion Zn anodes by regulating a bismuth-based energizer. *eScience* **2022**, *2*, 509–517.

[38] Ye, J. Q.; Ge, T. C.; Qu, X.; Mohideen, M. M.; Wang, C.; Hu, P.; Liu, Y. Spatial and electrostatic dual-confinement in hierarchical hollow Bi–Bi$_2$O$_3$@carbon nanofibers for dendrite suppression and side reaction mitigation in aqueous zinc-ion batteries. *Adv. Funct. Mater.* **2025**, *35*, 2425358.

[39] Li, T. T.; Hu, S. L.; Wang, C. G.; Wang, D.; Xu, M. W.; Chang, C. Y.; Xu, X. J.; Han, C. P. Engineering fluorine-rich double protective layer on Zn anode for highly reversible aqueous zinc-ion batteries. *Angew. Chem., Int. Ed.* **2023**, *62*, e202314883.

[40] Xin, W. L.; Xiao, J.; Li, J. W.; Zhang, L.; Peng, H. L.; Yan, Z. C.; Zhu, Z. Q. Metal–organic frameworks with carboxyl functionalized channels as multifunctional ion-conductive interphase for highly reversible Zn anode. *Energy Storage Mater.* **2023**, *56*, 76–86.

[41] Li, H. Y.; Li, Y.; Liu, M. Q.; Yang, Z. Y.; Gong, Y. T.; Qian, J.; Zhang, R. P.; Bai, Y.; Wu, F.; Wu, C. Biocrust-inspired interface layer with dual functions towards highly reversible zinc metal anodes. *Energy Environ. Sci.* **2025**, *18*, 2973–2984.

[42] Ma, L. T.; Li, Q.; Ying, Y. R.; Ma, F. X.; Chen, S. M.; Li, Y. Y.; Huang, H. T.; Zhi, C. Y. Toward practical high-areal-capacity aqueous zinc-metal batteries: Quantifying hydrogen evolution and a solid-ion conductor for stable zinc anodes. *Adv. Mater.* **2021**, *33*, 2007406.

[43] Dong, Y. Y.; Liu, F. Z.; Song, T.; Pei, Y.; Wang, X. Y.; Wu, X. W.; Chen, L. J.; Long, B. ZnNCN protective layer with high zincphilicity and ionic conductivity for stable zinc metal anodes. *Chem. Eng. J.* **2025**, *512*, 162630.

[44] Wang, Y. Q.; Zhu, Y. T.; Xian, H.; Wang, B.; Chen, Z.; Tan, X.; Wu, Z. Z.; Liu, S. L.; Mao, J. F.; Zhang, S. Q. et al. Amphiphilic fluorinated block copolymer additives for ultrastable aqueous Zn-ion batteries. *J. Am. Chem. Soc.* **2026**, *148*, 448–460.

[45] Shi, Z. H.; Yang, M.; Ren, Y. F.; Wang, Y. Z.; Guo, J. H.; Yin, J.; Lai, F. L.; Zhang, W. L.; Chen, S. L.; Alshareef, H. N. et al. Highly reversible Zn anodes achieved by enhancing ion-transport kinetics and modulating Zn (002) deposition. *ACS Nano* **2023**, *17*, 21893–21904.

[46] Zhao, L.; Li, Y.; Yu, M. M.; Peng, Y. Y.; Ran, F. Electrolyte-wettability issues and challenges of electrode materials in electrochemical energy storage, energy conversion, and beyond. *Adv. Sci.* **2023**, *10*, 2300283.

[47] Wang, H. C.; Zhu, M. Y.; Wang, H. B.; Li, C. X.; Ren, Z. J.; Zhang, Y. L.; Chen, S.; Li, H.; Chen, D. L.; Bai, Z. S. et al. Rearrangement of H-bonds network of solvation structure via a zincophilic polyol-type surfactant to stabilize zinc anode in aqueous zinc-ion batteries. *Energy Storage Mater.* **2024**, *67*, 103238.

[48] Ouyang, K. F.; Chen, S.; Ling, W.; Cui, M. W.; Ma, Q.; Zhang, K.; Zhang, P. X.; Huang, Y. Synergistic modulation of *in-situ* hybrid interface construction and pH buffering enabled ultra-stable zinc anode at high current density and areal capacity. *Angew. Chem., Int. Ed.* **2023**, *62*, e202311988.

[49] Wei, T. T.; Zhang, H.; Ren, Y. K.; Mo, L. E.; He, Y.; Tan, P.; Huang, Y.; Li, Z. Q.; Zhu, D. M.; Hu, L. H. Building near-unity stacked (002) texture for high-stable zinc anode. *Adv. Funct. Mater.* **2024**, *34*, 2312506.

[50] Luo, Z.; Xia, Y. F.; Chen, S.; Wu, X. X.; Akinlabi, E.; Xu, B. B.; Pan, H. G.; Yan, M.; Jiang, Y. Z. A homogeneous plating/stripping mode with fine grains for highly reversible Zn anodes. *Energy Environ. Sci.* **2024**, *17*, 6787–6798.

[51] Jeong, H. B.; Kim, D. I.; Yoo, G.; Mohan, D.; Roy, A.; Jung, M.; Jeong, H. S.; Cha, S. N.; An, G. H.; Cha, P. R. et al. Selective control of sharp-edge zinc electrodes with (002) plane for high-performance aqueous zinc-ion batteries. *J. Mater. Chem. A* **2024**, *12*, 15265–15277.

[52] Li, B.; Zhang, X. T.; Wang, T. T.; He, Z. X.; Lu, B. A.; Liang, S. Q.; Zhou, J. Interfacial engineering strategy for high-performance Zn metal anodes. *Nano-Micro Lett.* **2022**, *14*, 6.

[53] Wang, Z. L.; Wang, Y. H.; Py, B.; Maradesa, A.; Liu, J. P.; Wan, T. H.; Saccoccio, M.; Ciucci, F. DRTtools: Freely accessible distribution of relaxation times analysis for electrochemical impedance spectroscopy. *ACS Electrochem.* **2025**, *1*, 2680–2689.

[54] Zheng, X. H.; Han, B. B.; Liu, C. F.; Li, R. L.; Li, C. C.; Liu, S. K.; Wang, F. X.; Wu, Y. P. Taming zinc electrodeposition from the root to break zinc utilization/capacity barriers in practical zinc batteries. *Energy Environ. Sci.* **2026**, *19*, 1028–1041.

[55] Tang, M. C.; Liu, Q.; Zou, X. H.; Yu, Z. L.; Zhang, K. E.; Zhang, B.; An, L. Engineering *in-situ* heterometallic layer for robust Zn electrochemistry in extreme $Zn(BF_4)_2$ electrolyte environment. *Energy Storage Mater.* **2025**, *74*, 103896.

[56] Xue, T.; Mu, Y. B.; Zhang, Z. C.; Guan, J. P.; Qiu, J. H.; Yang, C.; Zang, L. M.; Zeng, L. Enhanced zinc deposition and dendrite suppression in aqueous zinc-ion batteries via citric acid-aspartame electrolyte additives. *Adv. Energy Mater.* **2025**, *15*, 2500674.

[57] Yu, H. M.; Chen, D. P.; Li, Q. Y.; Yan, C. S.; Jiang, Z. H.; Zhou, L. J.; Wei, W. F.; Ma, J. M.; Ji, X. B.; Chen, Y. J. et al. *In-situ* construction of anode-molecule interface via lone-pair electrons in trace organic molecules additives to achieve stable zinc metal anodes. *Adv. Energy Mater.* **2023**, *13*, 2300550.

[58] Yin, J. Y.; Liu, H. L.; Li, P.; Feng, X.; Wang, M. H.; Huang, C. Y.; Li, M. Y.; Su, Y. Q.; Xiao, B.; Cheng, Y. H. et al. Integrated electrolyte regulation strategy: Trace trifunctional tranexamic acid additive for highly reversible Zn metal anode and stable aqueous zinc-ion battery. *Energy Storage Mater.* **2023**, *59*, 102800.

[59] Wang, K.; Zhan, H. T.; Su, W. L.; Liu, X. X.; Sun, X. Q. Ordered interface regulation at Zn electrodes induced by trace gum additives for high-performance aqueous batteries. *Energy Environ. Sci.* **2025**, *18*, 1398–1407.

[60] Yan, M. D.; Dong, N.; Zhao, X. S.; Sun, Y.; Pan, H. L. Tailoring the stability and kinetics of Zn anodes through trace organic polymer additives in dilute aqueous electrolyte. *ACS Energy Lett.* **2021**, *6*, 3236–3243.

[61] Jiao, Z. Y.; Cai, X. X.; Wang, X. X.; Li, Y. R.; Bie, Z.; Song, W. X. Trace amount of nitrilotriacetate induced electrolyte evolution and textured surface for stable Zn anode. *Adv. Energy Mater.* **2023**, *13*, 2302676.

[62] Ouyang, K. F.; Li, F.; Ma, D. T.; Wang, Y. Y.; Shen, S. C.; Yang, M.; Qiu, J. M.; Wen, W. T.; Zhao, N.; Mi, H. W. et al. Trace-additive-mediated hydrophobic structure editing of aqueous zinc metal batteries for enabling all-climate long-term operation. *ACS Energy Lett.* **2023**, *8*, 5229–5239.

[63] Liu, K.; Sun, M. Z.; Wu, Y.; Zhang, T.; Zhu, A. Q.; Bu, S. Y.; Luan, C. H.; Liu, K. L.; Zhou, Y.; Lin, D. W. et al. Binary electrolyte additive-reinforced interfacial molecule adsorption layer for ultra-stable zinc metal anodes. *Adv. Mater.* **2025**, *37*, 2420079.

[64] Wang, X. R.; Wang, Y. L.; Naveed, A.; Li, G. T.; Zhang, H. W.; Zhou, Y.; Dou, A. C.; Su, M. R.; Liu, Y. J.; Guo, R. Q. et al. Magnesium ion doping and micro-structural engineering assist $NH_4V_4O_{10}$ as a high-performance aqueous zinc-ion battery cathode. *Adv. Funct. Mater.* **2023**, *33*, 2306205.